Frontiers of Physics
https://doi.org/10.1007/s11467-021-1134-1
Front. Phys.
17(4), 42501 (2022)

RESEARCH ARTICLE

Dynamics and formation of vortices collapsed from ring dark solitons in a two-dimensional spin–orbit coupled Bose–Einstein condensate

Peng-Hong Lu[1], Xiao-Fei Zhang[2,†], Chao-Qing Dai[1,‡]

[1] *College of Optical, Mechanical and Electrical Engineering, Zhejiang A&F University, Lin'an 311300, China*
[2] *Department of Physics, Shaanxi University of Science and Technology, Xi'an 710021, China*
Corresponding authors. E-mail: †xfzhang_physics@163.com, ‡dcq424@126.com
Received September 9, 2021; accepted November 18, 2021

We consider the dynamics and formation of vortices from ring dark solitons in a two-dimensional Bose–Einstein condensate with the Rashba spin–orbit coupling based on the time-dependent coupled Gross–Pitaevskii equation. Compared with previous results, the system exhibits complex dynamical behaviors in the presence of the spin–orbit coupling. With the modulation of the spin–orbit coupling, not only the lifetime of ring dark solitons is greatly prolonged, but also their attenuation kinetics is significantly affected. For two shallow ring dark solitons with the equal strength of the spin–orbit coupling, the radius of ring dark solitons increases to a maximum value over time and then shrinks into a minimum value. Due to the effect of the snake instability, ring dark solitons split into a series of ring-like clusters of vortex pairs, which perform complex oscillations. This indicates that the system is strongly dependent on the presence of the spin–orbit coupling. Furthermore, the effect of different initial modulation depths on the dynamics of ring dark solitons is investigated.

Keywords Bose–Einstein condensate, Rashba spin–orbit coupling, ring dark solitons, vortex pairs

1 Introduction

Over the past decades, the condensates of ultra-cold atoms have proved to be an ideal platform for the exploration of superfluid [1–3] . Due to the change of internal degrees of freedom, multi-component Bose–Einstein condensates (BECs) can produce more abundant nonlinear excitations and more complex dynamic behaviors than one-component BEC (scalar condensate) [4–6], such as a variety of vector solitons [7], self-bound three-dimensional solitons [8, 9], and self-trapped quantum balls [10]. With the introduction of ring dark solitons (RDSs) from nonlinear optics into ultra-cold atomic systems [11], the generation, modulation and kinetic behaviors of RDSs in one-component and two-component systems have been well studied [12–14]. RDSs can be used to generate quantum turbulence, thus it will help to understand the statistical properties of quantum turbulence and its inherent physical mechanism.

Recently, the successful implementation of artificial spin–orbit coupling (SOC) experiments in ultra-cold atomic systems has greatly expanded the field of ultra-cold atomic gases for quantum simulation [15–17]. The realization of gauge potential field and SOC in the cold atom open up a new field, which makes the cold atom as an important physical simulation platform easy to understand and simulate a large number of gauge field-related physical phenomena [18]. Ultra-cool atomic systems with SOC have shown fascinating value in quantum simulations. Artificial SOC breaks through the bottleneck that neutral atoms cannot simulate the response of charged particles to the external electromagnetic field [19, 20]. It provides the possibility for the discovery of new state of matter [21], and has a greater application potential in the fields of quantum simulation, quantum information and quantum computing [22–24].

The stability mechanism of RDSs in the system comes from the balance between the diffusion caused by SOC and the attracted nonlinear term [25, 26]. However, the dynamics of the two RDSs in the SOC two-component BECs has hardly been reported in previous literatures. Therefore, we study the effects of system parameters, such as contact interaction, eccentricity, and boundary value conditions, on the dynamics of RDSs in the SOC two-component BEC system. We find that various types of vortex structures and patterns can be generated by the decay of RDSs, which provides a new idea to further study of vortex dynamics, pattern dynamics and other nonlinear phenomena in BECs.

In the present paper, we consider a binary SOC BEC confined in a quasi-two-dimensional (2D) axisymmetric

* This article can also be found at http://journal.hep.com.cn/fop/EN/10.1007/s11467-021-1134-1.

trap, which can be achieved by adding very strong harmonic limits along the axis-direction. By directly solving the time-dependent coupled Gross–Pitaevskii (GP) equation, the dynamics of the two RDSs and the vortices generated by the collapse of the RDSs are studied numerically in detail. In the presence of SOC, with the evolution of time, the radius of the RDSs first increases to a maximum, then gradually decreases and oscillates at the minimum radius. Moreover, the lifespan of RDSs is significantly longer than the lifespan of RDSs for systems without SOC. We find that there are half quantum vortex dipoles in the system, in which the nucleus of the vortex–antivortex pair in one component are occupied by the other component [27]. Moreover, the vortex pairs exhibit complex dynamic behaviors, including their separation and recombination, and show strong dependence on the SOC, contact interaction, eccentricity and initial depth of the RDS.

The rest of the present paper is organized as follows. In Section 2, we introduce the theoretical description of the SOC pseudospin-1/2 BECs confined in a harmonic potential. In Section 3, according to the mean field approximation principle, the effects of different system parameters on the dynamics of RDSs and the vortices generated by the RDSs oscillation are studied. In the last section, the main results of this paper are summarized.

2 The model

We consider a 2D pseudospin-1/2 BEC with the Rashba SOC. According to the mean field approximation principle, the system can be described by the spin order parameter $\psi(r) = (\psi_1(r), \psi_2(r))^{\mathrm{T}}$, where T stands for the transposition. The dynamical behavior of the system follows the coupled GP equation [28–30]:

$$\begin{aligned}
\mathrm{i}\hbar\frac{\partial\psi_1}{\partial t} &= \left[-\frac{\hbar^2}{2m}\nabla^2 + g_{11}\left|\psi_1\right|^2 + g_{12}\left|\psi_2\right|^2 \right.\\
&\quad \left. + V(r,z)\right]\psi_1 + \mathrm{i}\frac{\hbar\kappa}{m}\nabla\cdot\sigma_\perp\psi_2,\\
\mathrm{i}\hbar\frac{\partial\psi_2}{\partial t} &= \left[-\frac{\hbar^2}{2m}\nabla^2 + g_{22}\left|\psi_2\right|^2 + g_{21}\left|\psi_1\right|^2 \right.\\
&\quad \left. + V(r,z)\right]\psi_2 + \mathrm{i}\frac{\hbar\kappa}{m}\nabla\cdot\sigma_\perp\psi_1,
\end{aligned} \tag{1}$$

where the condensate wave function ψ_j denotes the wave function of the j th $(j = 1, 2)$ component, and they satisfy the normalization condition of $N = \int\left(\left|\psi_1\right|^2 + \left|\psi_2\right|^2\right)\mathrm{d}r\mathrm{d}z$. Here m is the atomic mass, κ is the strength of the SOC, and $\sigma_\perp(\sigma_x, \sigma_y, 0)$ are the 2×2 Pauli matrices. The contact interaction parameters within the intra- and inter-component coupling constants are respectively expressed as g_{11}, g_{22} and $g_{12} = g_{21}$ with $g_{ij} = 4\pi a_{ij}\hbar^2/m$ and $g_{3-i,j} = 4\pi a_{3-i,j}\hbar^2/m, a_{jj}$ and $a_{3-j,j}$ are the scattering length of s-wave between atoms, which can be controlled by the Feshbach resonance technique. The external potential of the system can be expressed as $V(r,z) = m\left(\omega_r^2 r^2 + \omega_z^2 z^2\right)/2$, where ω_r and $\omega_z, r^2 = x^2 + y^2$ are axial constraint frequencies and the radial respectively.

Further assuming that ω_z is much larger than ω_r, which means that there is a very strong constraint along the z axis. In this case, the wave function can be equivalent to $\psi_j(r,z,t) = \psi_j(x,y,t)f(z)$. After integrating out the axial coordinate, the radial wave functions satisfy the following dimensionless coupled GP equation:

$$\begin{aligned}
\mathrm{i}\frac{\partial\psi_1}{\partial t} &= \left(-\frac{1}{2}\nabla^2 + g_{11}\left|\psi_1\right|^2 + g_{12}\left|\psi_2\right|^2 \right.\\
&\quad \left. + \frac{1}{2}\Omega^2 r^2\right)\psi_1 - \kappa\left(\mathrm{i}\frac{\partial}{\partial x} + \frac{\partial}{\partial y}\right)\psi_2,\\
\mathrm{i}\frac{\partial\psi_2}{\partial t} &= \left(-\frac{1}{2}\nabla^2 + g_{22}\left|\psi_2\right|^2 + g_{21}\left|\psi_1\right|^2 \right.\\
&\quad \left. + \frac{1}{2}\Omega^2 r^2\right)\psi_2 + \kappa\left(-\mathrm{i}\frac{\partial}{\partial x} + \frac{\partial}{\partial y}\right)\psi_1,
\end{aligned} \tag{2}$$

where we work in natural units and let $\hbar = m = 1, \nabla^2 = \partial^2/\partial x^2 + \partial^2/\partial y^2, \Omega = \omega_r/\omega_z$. The units of length and time are chosen as $a_z = \sqrt{\hbar/(m\omega_z)}$ and $1/\omega_z$, respectively. The kinetic and SOC energies are given by

$$\begin{aligned}
E_1 = \iint\Bigg[&-\frac{1}{2}\psi_1^*\nabla^2\psi_1 - \frac{1}{2}\psi_2^*\nabla^2\psi_2\\
&+ \kappa\psi_1^*\left(-\mathrm{i}\frac{\partial}{\partial x} - \frac{\partial}{\partial y}\right)\psi_2\\
&+\kappa\psi_2^*\left(-\mathrm{i}\frac{\partial}{\partial x} + \frac{\partial}{\partial y}\right)\psi_1\Bigg]\mathrm{d}x\mathrm{d}y.
\end{aligned} \tag{3}$$

The external potential energies and the s-wave contact interaction energy is written as

$$\begin{aligned}
E_2 = \iint\Bigg(&\frac{1}{2}g_{11}\left|\psi_1\right|^4 + \frac{1}{2}g_{22}\left|\psi_2\right|^4 + g_{12}\left|\psi_1\right|^2\left|\psi_2\right|^2\\
&+\frac{1}{2}\psi_1^*\Omega^2 r^2\psi_1 + \frac{1}{2}\psi_2^*\Omega^2 r^2\psi_2\Bigg)\mathrm{d}x\mathrm{d}y,
\end{aligned} \tag{4}$$

and the total energy is given by $E = E_1 + E_2$.

We study the dynamics of the system described in Eq. (2) by using the the time-splitting Fourier spectral method. Meanwhile, in order to study the effects of contact interactions between components on system dynamics, we fix the intra-component coupling constants as $g_{11} = g_{22} = 1$, corresponding to the SU(2) contact interactions. We choose two appropriate approximate solutions where each component contains an RDS with an initial radius

$$\psi_j(x,y,0) = \left(1 - \frac{\Omega^2 r^2}{4}\right)[\cos\varphi_j(0)$$

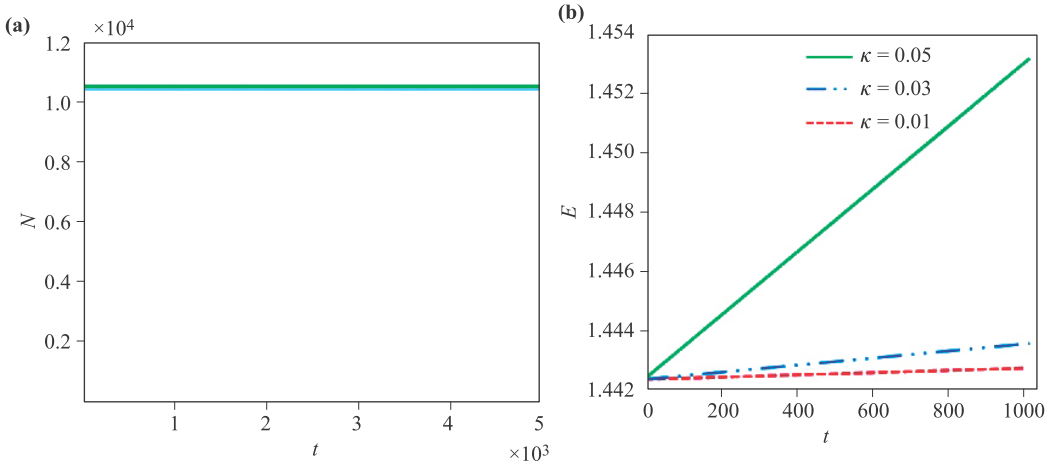

Fig. 1 **(a)** The change of particle number with time when the strength of SOC is 0.01. **(b)** The change of total energy of the system with time when the strength of SOC is different.

$$\times \tanh Z(r_1) + \mathrm{i}\sin\varphi_j(0)]\,\mathrm{e}^{\mathrm{i}\kappa x}, \tag{5}$$

where $\cos\varphi_j(0)$ determines the initial depth of the RDS, $Z(r_1) = (r_1 - R_{j0})\cos\varphi_j(0), r_1 = \sqrt{(1-e_c^2)\,x^2 + y^2}$ and e_c represents the eccentricity of the ring. When the value of e_c is not zero, R_{j0} denotes the length of the semiminor axis of the elliptical configuration. Particularly, the ground state of a SOC system is the plane-wave state for $g_{12}/g_{11} < 1$ and the stripe state for $g_{12}/g_{11} > 1$. In what follows, we focus on $g_{12}/g_{11} \leq 1$ and the plane-wave is given by $\psi_j(r) = \mathrm{e}^{\mathrm{i}\kappa x}$.

Before the analysis begins, we first give the changes of the total number of particles in the evolution process. As shown in Fig. 1(a), the corresponding case is the change of the number of particles with $\kappa = 0.01$. Obviously, the number of particles in the evolution process is always conserved. Then we calculate that the number of particles for different κ are always conserved. But as shown in Fig. 1(b), different κ corresponds to different total energy of the system. When the value of κ is small, the total energy of the system does not change significantly. However, as κ increases, the total energy of the system increases rapidly. This indicates that as κ increases, the error of numerical calculation increases, which affects the accuracy of the conclusions. Therefore, we choose a smaller value $\kappa = 0.01$.

The results are converted into data relevant to the experiment. The most promising binary system can be realized by selecting $|F = 1, m_F = 0\rangle$ and $F = 2, m_F = 1\rangle$ spin state of ^{87}Rb. The atoms in the system are confined by a disk-shaped trap with radial frequency $\Omega_\perp = 2\pi \times 18$ Hz and axial frequency $\Omega_z = 2\pi \times 628$ Hz [31]. Therefore, the unit of time is 0.25 ms, the unit of length is 0.42 μm, and the aspect ratio of the harmonic potential is $\Omega = 0.028$. The intracomponent interactions are $g_{11} = g_{22} = c_0, g_{12} = g_{21} = c_0 + c_2$, where $c_0 = 7.79\times10^{-12}$ Hz·cm^3, $c_2 = -3.61\times10^{-14}$ Hz·cm^3. The initial radii of the two RDS are $R_{10} = 11.95$ μm, $R_{20} = 12.38$ μm. Furthermore, the initial states of two different ring dark solitons can be achieved by using remote resonant laser pulses to imprint different phases on the two components.

3 RDS dynamics and vortex pairs

In this section, we will numerically study the dynamic behaviors of RDSs with the circular symmetry. The richness of the present system lies in the fact that it can regulate a large number of free parameters. In what follows, we mainly focus on the effects of contact interaction, initial depth, eccentricity and boundary value conditions, on the dynamical characteristics of two RDSs and the vortices generated after the collapse of the RDSs.

Without loss of generality, we try to simplify the situation by fixing $\Omega = 0.028$, and assume the equal initial depths $\cos\varphi_1(0) = \cos\varphi_2(0)$ and the radii of the elliptic short axes $R_{10} = 27.9$ and $R_{20} = 28.9$. Here the radius difference is $\Delta R = 1$, which can ensure the collisions of RDSs and the followed dynamics of vortices. Expressly, our numerical results show that there exists a critical value of the SOC, $\kappa_{\max} = 0.03$, above which the system becomes unstable in a very short time interval. To highlight the effect of the SOC and avoid this instability, we set $\kappa = 0.01$ throughout this paper. The field of view is taken to be 300×300, which is large enough to ensure that the boundary conditions have little effect on the system.

3.1 The effects of contact interactions on the dynamics of RDS

First of all, we consider the system with a small intercomponent interaction with $g_{21} = g_{12} = 0.5$ and the equal initial depths $\cos\varphi_1(0) = \cos\varphi_2(0) = 0.6$. Figure 2 shows

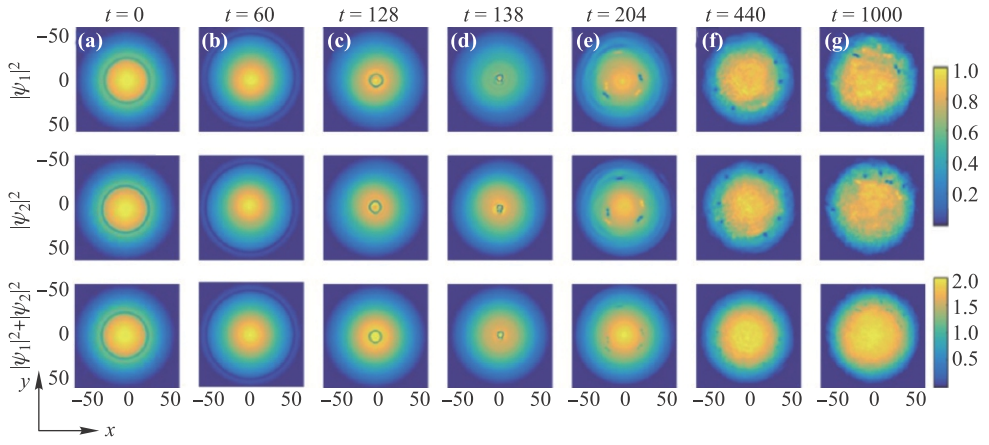

Fig. 2 The time evolutions of two RDSs at a two-component BEC with the SOC for a small inter-component interaction $g_{12} = g_{21} = 0.5$ at **(a)** $t = 0$, **(b)** $t = 60$, **(c)** $t = 128$, **(d)** $t = 138$, **(e)** $t = 204$, **(f)** $t = 440$, and **(g)** $t = 1000$. The first and second rows represent the densities of component 1 and component 2 respectively. The bottom row is the corresponding total density. The initial depths of two RDSs $\cos\varphi_1(0) = \cos\varphi_2(0) = 0.6$, the trap frequency $\Omega = 0.028$, eccentricity $e_c = 0$, and the initial locations $R_{10} = 27.9$ and $R_{20} = 28.9$.

the following dynamics of two RDSs with the circular symmetry, viz., $e_c = 0$. Patterns in the first and second rows represent the density of component 1 and component 2 respectively, and patterns in the bottom row is the total density.

In order to describe the dynamical evolution behavior of RDSs clearly, the corresponding one-dimensional density distributions are given simultaneously in Fig. 3. Figures 2(a) and 3(a) show the typically initial profiles of such two RDSs. The position of RDS is -27.9 at the initial time $t = 0$, -41.3 at $t = 16$, and -52.9 at $t = 60$, but the position transfer to -4.7 at $t = 138$. Different from the system without the SOC [27], the initial RDSs will first increase to a maximum at $t = 60$, as shown in Figs. 2(b) and 3(c). With the evolution of time, the radii of the RDSs gradually decrease to a minimum value at $t = 138$ [see Figs. 3(b) and (d)]. At this point, the symmetry of the rings is broken, and they become the irregular patterns [see Fig. 2(d)].

Interestingly, the radii of RDSs maintain circular symmetry until they are minimized at $t = 138$. This indicates that the presence of the SOC increases the lifetime of RDSs, which is defined as the time interval between the start and the time point when the snaking instability occurs [31]. This phenomenon can be understood by the fact that the stabilization mechanism of the RDSs come from the balance between dispersion induced by the SOC and nonlinearity. With the development of the snake instability, RDSs gradually disappear and develop into a series of solitary waves [see Fig. 2(e)].

We notice that dynamical behaviors above mentioned are different from the system without the SOC. In this case without the SOC, as reported in Ref. [27], the RDSs shrinked but they did not oscillate. Moreover, as reported in Ref. [14], the RDSs oscillated in the system without the SOC in the presence of the periodic modulation of the inter-component interaction, during which new gray RDSs were created.

As shown in Figs. 2(e) and (f), two such solitary waves move outward in the radial direction and then develop into half-quantum vortex dipoles, where the density difference of the half-quantum vortex dipole cores satisfies $\Delta n = |\psi_1|^2 - |\psi_2|^2 \neq 0$. Subsequently, the vortex and anti-vortex within the half-quantum vortex dipoles separate each other and move along the edges of the condensate [see Fig. 2(f)], during which they form new half-quantum vortex dipoles. The underlying physics lies in the fact that its density gradient points to the center of the condensate for the condensate in the harmonic oscillator trap. When a vortex (anti-vortex) is located outside the center of the harmonic oscillator, the direction of the velocity change of the vortex (anti-vortex) that makes up the vortex pair is always perpendicular to the radius of the condensate. Therefore, the vortex (anti-vortex) will process around the condensate in a counterclockwise (clockwise) direction [32–34], leading to the separation of vortex pairs. When the separated vortex meets with anti-vortex in the precession process, a new half-quantum vortex dipole will be formed, and then the half-quantum vortex dipole will be developed into vortex and anti-vortex in a very short time. This process is then repeated until the vortices are completely dissipated from the condensate [see Fig. 2(g)]. Figures 4(a) and (c) show the initial density and phase of RDS for the component 2, respectively. Figures 4(b) and (d) show the density and phase diagrams of vortex and antivortex pairs, respectively. In order to see the vortex and anti-vortex clearly, we enlarged the local image. The red circle in Fig. 4(d) is the pair of vortex and anti-vortex in the red circle in Fig. 4(b).

Next, we consider the critical case with $g_{21} = g_{12} = 1$

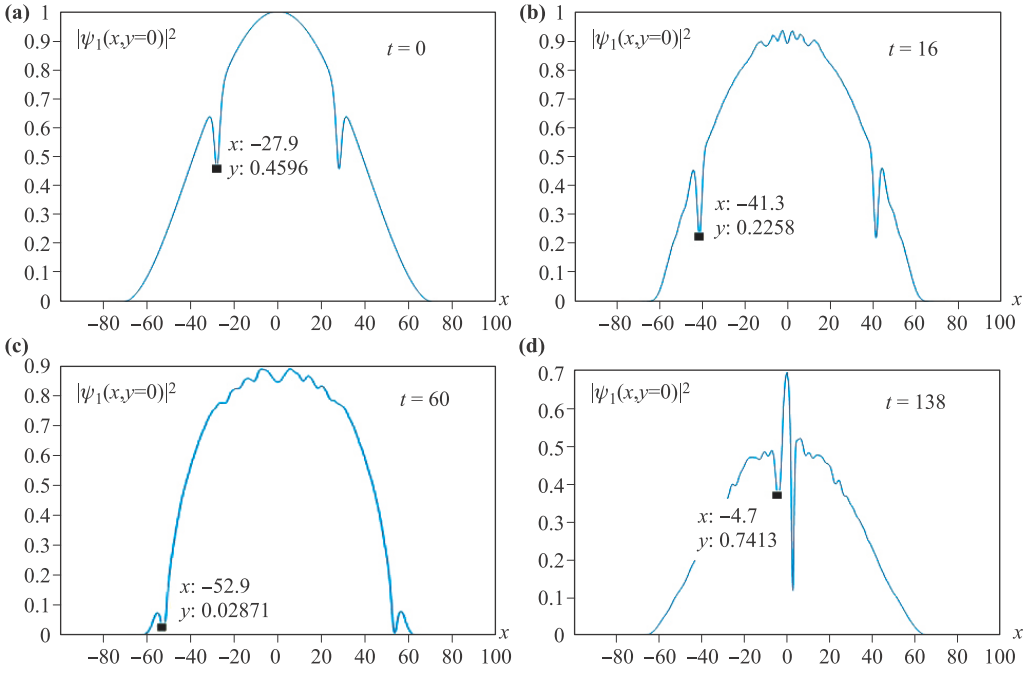

Fig. 3 The 1D density distributions of the component ψ_1 at **(a)** $t = 0$, **(b)** $t = 16$, **(c)** $t = 60$, **(d)** $t = 138$, respectively. Other parameters are same as that in Fig. 2.

for the equal initial depths $\cos\varphi_1(0) = \cos\varphi_2(0) = 0.6$. Compared with the previous situation, the RDSs reach minimum radii at $t = 135$. During the later evolution, they become relatively shallow elliptical dark solitons and their radii increase slowly, then the elliptical dark solitons disappear and develop into half-quantum vortex dipoles [see Figs. 5(c) and (d)]. We recall that after $t = 138$ in Fig. 1, the RDSs disappear completely, then directly decay into half-quantum vortex dipoles, and no shallow elliptical RDSs form. This can be understood by the fact that the larger inter-component interaction balances the instability of RDSs induced by the SOC, and thus makes RDSs more stable and not easy to collapse. This indicates that the lifetime of the RDSs under the larger inter-component interaction is slightly longer. In Fig. 5(g), with the development of instability, both components develop into two pairs of vortices. Similarly, as the system evolves, the vortices and anti-vortices in the half-quantum vortex dipoles of the system are separated. After then these vortices and anti-vortices in the system are recombined until they completely disappear from the condensate.

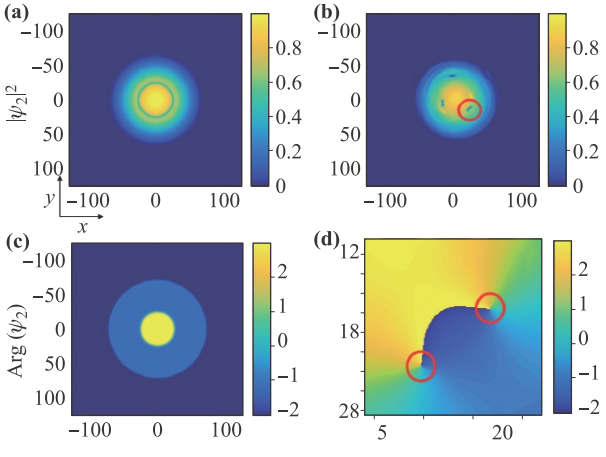

Fig. 4 Corresponding density and phase diagrams of component $2\psi_2$ in Figs. 2(a) and (e). Other parameters are same as that in Fig. 2.

Compared with the case of small inter-component interaction $g_{12} = g_{21} = 0.5$ in Fig. 2(e) the numbers of vortex pairs generated from the collapses of RDSs reduce in Fig. 5(e), although the trajectories of these vortex pairs are essentially unchanged. Consequently, the number of vortex pairs produced by the decay of RDSs shows a strong dependence on the contact interactions between such two components. More interesting, at the center of the condensate in Fig. 5(e), there appear some gray RDSs, which do not appear in Fig. 2(e), and these gray RDSs gradually move towards the center and disappear. The reason for these phenomena may be that the effect of SOC makes these gray RDSs appear in the beginning, and the interactions between these gray RDSs cancel out part of the SOC effect and make these gray RDSs disappear ultimately. As reported in Ref. [14], the system without the SOC in the presence of periodic modulation of the inter-component interaction also appears new shallower RDSs and forms a series of concentrically annular RDSs.

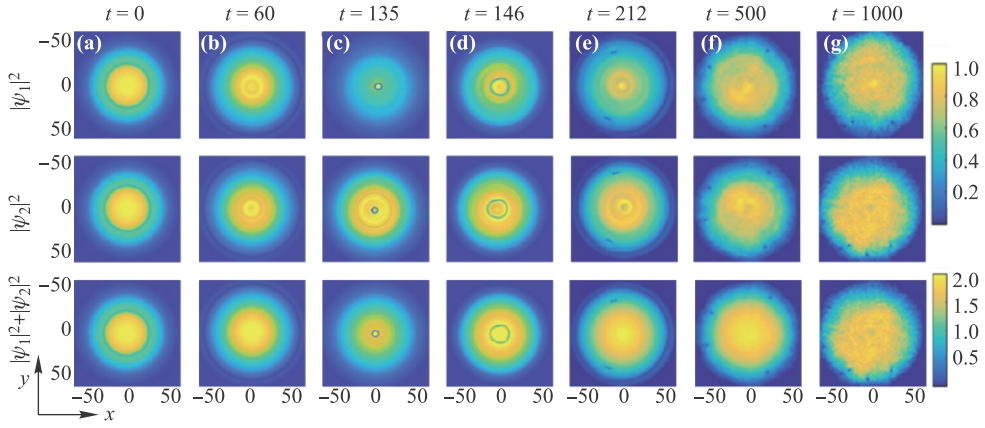

Fig. 5 The time evolutions of two RDSs in a BEC with the SOC at **(a)** $t = 0$, **(b)** $t = 60$, **(c)** $t = 135$, **(d)** $t = 146$, **(e)** $t = 212$, **(f)** $t = 500$, and **(g)** $t = 1000$. The initial inter-component interactions of two RDSs are $g_{12} = g_{21} = 1$. Other parameters are same as that in Fig. 2.

3.2 The effects of eccentricity on the dynamics of RDS

We discuss the dynamics of RDSs with nonzero eccentricity, viz., $e_c = 0.4$, and we fix the inter-component interactions $g_{12} = g_{21} = 1$, and the equal initial depths $\cos\varphi_1(0) = \cos\varphi_2(0) = 0.6$. In this case, it is interesting to see that the RDSs are compressed into elliptical dark solitions at $t = 130$ [see Fig. 6(c)]. With the development of snake instability, they develop into two half-quantum vortex dipoles accompanied by shallow elliptical dark solitons. The elliptical dark solitons oscillate when they reach the edge of the condensate, and then also develop into two half-quantum vortex dipoles [see Figs. 6(d) and (e)]. At this time, each component contains four half-quantum vortex dipoles. Similar to the previous results, the vortices and anti-vortices of the half-quantum vortex dipoles perform separation and recombination, and move along the edge of the condensate until they are completely dissipated from the condensate [see Figs. 6(f) and (g). Compared with the results in Figs. 5(c) and (d), the elliptical disturbance has a certain effect on this system. The lifetime of RDS is slightly reduced. When RDSs develop into elliptic dark solitons, their radii do not increase, but develop into four half-quantum vortex dipoles [see Figs. 6(c) and (d). The number of half-quantum vortex dipoles here has increased significantly [see Fig. 6(e)].

3.3 The effects of larger initial depths on the dynamics of RDS

We explore the influence of different initial modulation depths on the dynamics of RDS. Figures 7(a) and (b) show the density of component 1 and component 2 at $t = 130$ and $t = 190$ respectively for the initial depths $\cos\varphi_1(0) = \cos\varphi_2(0) = 0.75$ and initial inter-component interactions $g_{12} = g_{21} = 1$. When $t = 130$, RDS oscil-

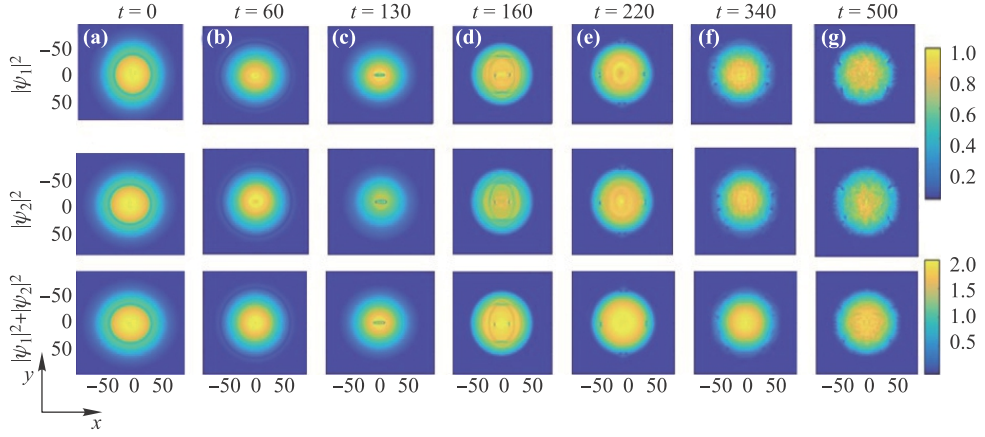

Fig. 6 The time evolutions of two RDSs in a two-component BEC with the SOC at **(a)** $t = 0$, **(b)** $t = 60$, **(c)** $t = 130$, **(d)** $t = 160$, **(e)** $t = 220$, **(f)** $t = 340$, and **(g)** $t = 500$. The eccentricity of two RDSs is $e_c = 0.4$. Other parameters are same as that in Fig. 4.

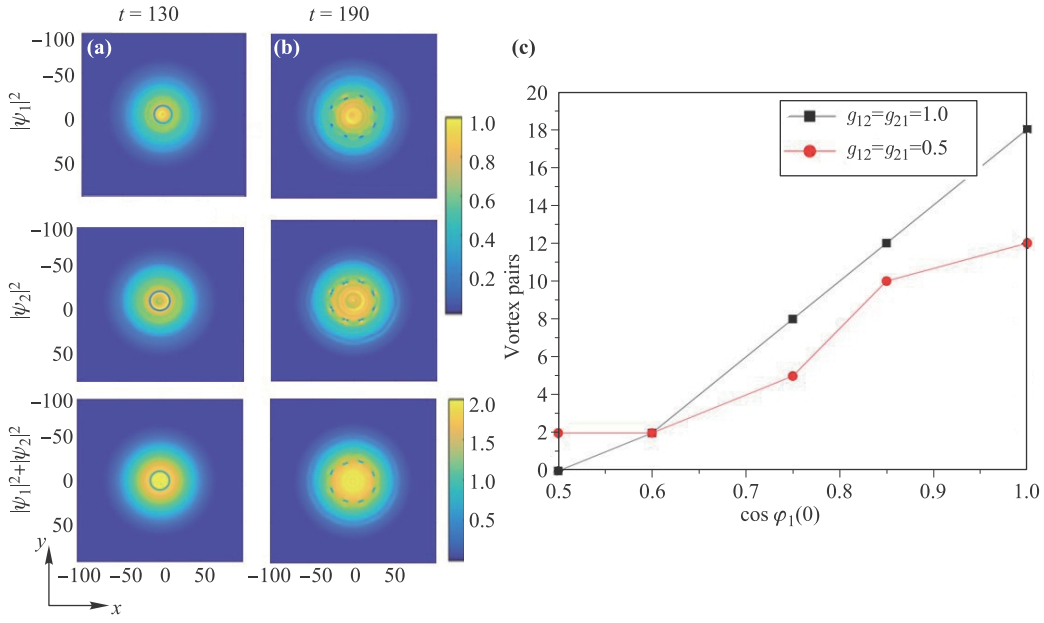

Fig. 7 The time evolutions of two RDSs in a two-component BEC with the SOC at **(a)** $t = 130$ and **(b)** $t = 190$ for the initial depths of two RDSs $\cos\varphi_1(0) = \cos\varphi_2(0) = 0.75$ and the initial intercomponent interaction $g_{12} = g_{21} = 1.0$. **(c)** The number of vortex pairs generated in the decay process of RDSs vs. the initial depth for the different inter-component interactions with $g_{12} = g_{21} = 1.0$ (black curve) and $g_{12} = g_{21} = 0.5$ (red curve). Other parameters are same as that in Fig 2.

lates and gradually decays to 8 pairs of vortices, and the number of vortex pairs at $t = 190$ is significantly more than that in Figs. 3(e)–(g). Theocharis *et al.* [32] have firstly studied the decay dynamics of ring dark solitons for a single-component BEC, where the number of vortex pairs is always a multiple of 4, and after a long time of evolution, some vortex pairs annihilated, leaving only 4 vortex–antivortex pairs stable for a long time. Wang *et al.* [27] have found that the decay of RDSs in a two-component BEC produced vortex pairs that are odd times of 2. However, in the presence of SOC, the number of vortex pairs generated by RDSs does not satisfy these laws above.

In Fig. 7(c), we show the number of vortex pairs generated by RDSs for different modulation depths with the inter-component interaction $g_{12} = g_{21} = 1$. When the initial depth of RDS $\cos\varphi_1(0) = 0.5$, no vortex pairs are generated in the decay process of RDS. When the modulation depth exceeds 0.6, the number of vortex pairs increases linearly with the increase of the initial modulation depth, which shows strong dependence on the initial modulation depth. However, for the small inter-component interaction $g_{12} = g_{21} = 0.5$, two vortex pairs will be generated at initial depth $\cos\varphi_1(0) = 0.5$, which indicates that the generation of vortex pairs is related to the competition between the contact interactions and initial depth.

It is interesting to see that there exists a critical value of initial depth, namely $\cos\varphi_1(0) = \cos\varphi_2(0) = 0.75$, above which the lifespan of the RDS is significantly shortened. In such cases, the RDSs will oscillate due to the serpentine instability in the increasing process of their radii, and finally decay into many vortex pairs. This also proves that the deeper the initial modulation depth is, the more obvious the instability of RDS is. Thus, we conclude that the number of vortex pairs generated by RDS splitting adds with the increase of initial depth when the initial depth of RDS in two components is same. The deeper the initial depth, the more vortices are generated by the oscillation. A shallow RDS with circular symmetry will decay relatively slowly, while a ring black soliton is more prone to the snakelike instability. In particular, we show through extensive numerical studies that the dynamical behavior of the RDSs and the formation of the vortices are similar to our results when the strength of SOC has small variation.

Finally, we study the influence of boundary conditions on the dynamics of the system. It is well known that the accuracy of the numerical results shows strong dependence on the boundary conditions and the interval of numerical calculation [11]. The square calculation region we use will introduce certain symmetry, and the initial state of RDSs and their periodic boundary conditions we choose together determine the symmetric structure of the system in the decay process [35, 36]. Further, it is noted that the numerical method using the artificial square calculation region in the study of RDSs dynamics does not affect the results [37]. Therefore, we enlarge the numerical calculation area twice, choose the unequal space step, and repeat the numerical simulations. Our results show that the mainly physical pictures are unchanged. Typically, we

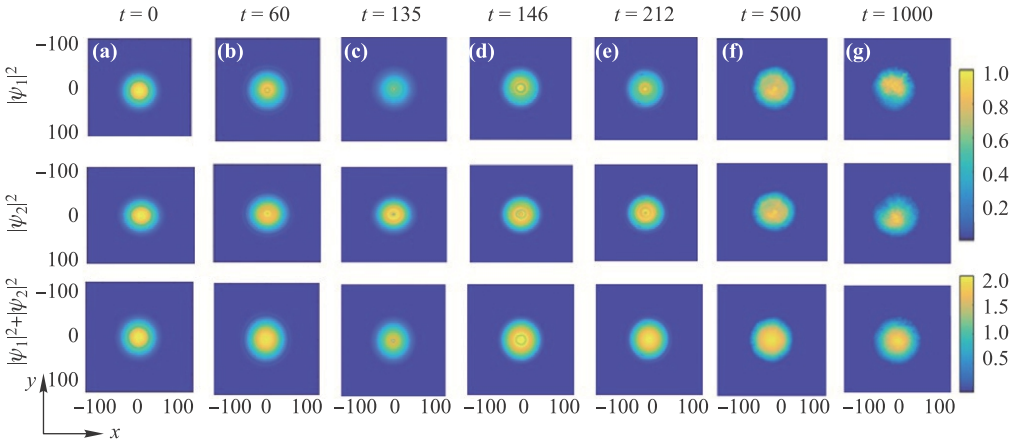

Fig. 8 The time evolutions of two RDSs in a two component BEC with the SOC at **(a)** $t = 0$, **(b)** $t = 60$, **(c)** $t = 135$, **(d)** $t = 146$, **(e)** $t = 212$, **(f)** $t = 500$, and **(g)** $t = 1000$ for a larger computational box (specially, twice the size of Fig. 3). Other parameters are same as that in Fig. 3.

take Fig. 5 as an example to repeat the numerical simulations. Figure 8 shows the dynamical evolution process of two RDSs in a large numerical calculation area for the same parameters as those in Fig. 5. Compared these results in Figs. 5 and 8, we can't see the essential difference.

4 Conclusion

In summary, we study the dynamics of RDSs in 2D BEC with the SOC and the formation of vortices generated by RDS collapse. In the presence of SOC, the effects of the inter-component components and the eccentricity on the dynamics of RDSs and vortex pairs are investigated. Compared with the system without SOC, the presence of SOC greatly extended the lifetime of the RDS, and the dynamics of the system exhibits exotic dynamics behavior, where the radius of the RDS first increases to a maximum and then gradually decreases to a minimum. Moreover, we find that half-quantum vortex dipoles generated during the decay process exhibit multiple recombination until they are completely dissipated from the condensate, and its number shows a strong dependence on the eccentricity and the inter-component interaction.

Acknowledgements This work was supported by the Zhejiang Provincial Natural Science Foundation of China (Grant No. LR20A050001), the National Natural Science Foundation of China (Grant Nos. 12075210 and 12175129), and the Scientific Research and Developed Fund of Zhejiang A&F University (Grant No. 2021FR0009).

References

1. M. Ota, S. Giorgini, and S. Stringari, Magnetic phase transition in a mixture of two interacting superfluid Bose gases at finite temperature, *Phys. Rev. Lett.* 123(7), 075301 (2019)
2. Y. R. Shi, X. L. Wang, G. H. Wang, C. B. Liu, Z. G. Zhou, and H. J. Yang, Analytical solutions for the spin-1 Bose–Einstein condensate in a harmonic trap, *Front. Phys.* 8(3), 319 (2013)
3. R. X. Zhong, Z. P. Chen, C. Q. Huang, Z. H. Luo, H. S. Tan, B. A. Malomed, and Y. Y. Li, Self-trapping under two-dimensional spin–orbit coupling and spatially growing repulsive nonlinearity, *Front. Phys.* 13(4), 130311 (2018)
4. X. F. Zhang, X. H. Hu, D. S. Wang, X. Liu, and W. Liu, Dynamics of Bose–Einstein condensates near Feshbach resonance in external potential, *Front. Phys.* 6(1), 46 (2011)
5. S. B. Prasad, B. C. Mulkerin, and A. M. Martin, Stationary states, dynamical stability, and vorticity of Bose–Einstein condensates in tilted rotating harmonic traps, *Phys. Rev. A* 101(6), 063608 (2020)
6. Z. X. Niu and W. Zhang, Spontaneous formations of dynamical steady states in polariton condensates, *Front. Phys.* 9, 696278 (2021)
7. J. Yang and Y. Tan, Fractal structure in the collision of vector solitons, *Phys. Rev. Lett.* 85(17), 3624 (2000)
8. X. Gao and J. Zeng, Two-dimensional matter-wave solitons and vortices in competing cubic–quintic nonlinear lattices, *Front. Phys.* 13(1), 130501 (2018)
9. L. M. Zhao, D. Y. Tang, H. Zhang, X. Wu, C. Lu, and H. Y. Tam, Period-doubling of vector solitons in a ring fiber laser, *Opt. Commun.* 281(22), 5614 (2008)
10. S. Middelkamp, J. J. Chang, C. Hamner, R. Carretero-González, P. G. Kevrekidis, V. Achilleos, D. J. Frantzeskakis, P. Schmelcher, and P. Engels, Dynamics of dark–bright solitons in cigar-shaped Bose–Einstein condensates, *Phys. Lett. A* 375(3), 642 (2011)
11. L. Wen, H. Guo, Y. J. Wang, A. Y. Hu, H. Saito, C. Q. Dai, and X. F. Zhang, Effects of atom numbers on the miscibility-immiscibility transition of a binary Bose–Einstein condensate, *Phys. Rev. A* 101(3), 033610 (2020)

12. Y. J. Wang, L. Wen, G. P. Chen, S. G. Zhang, and X. F. Zhang, Formation, stability, and dynamics of vector bright solitons in a trapless Bose–Einstein condensate with spin–orbit coupling, *New J. Phys.* 22(3), 033006 (2020)
13. M. Kato, X. F. Zhang, D. Sasaki, and H. Saito, Twisted spin vortices in a spin-1 Bose–Einstein condensate with Rashba spin–orbit coupling and dipole–dipole interaction, *Phys. Rev. A* 94(4), 043633 (2016)
14. Z. M. He, L. Wen, Y. J. Wang, G. P. Chen, R. B. Tan, C. Q. Dai, and X. F. Zhang, Dynamics and pattern formation of ring dark solitons in a two-dimensional binary Bose–Einstein condensate with tunable interactions, *Phys. Rev. E* 99(6), 062216 (2019)
15. Y. J. Lin, K. Jimenez-Garcia, and I. B. Spielman, Spin–orbit-coupled Bose–Einstein condensates, *Nature* 471(7336), 83 (2011)
16. Z. Wu, L. Zhang, W. Sun, X. T. Xu, B. Z. Wang, S. C. Ji, Y. Deng, S. Chen, X. J. Liu, and J. W. Pan, Realization of two-dimensional spin–orbit coupling for Bose–Einstein condensates, *Science* 354(6308), 83 (2016)
17. Z. Y. Wang, X. C. Cheng, B. Z. Wang, J. Y. Zhang, Y. H. Lu, C. R. Yi, S. Niu, Y. Deng, X. J. Liu, S. Chen, and J. W. Pan, Realization of an ideal Weyl semimetal band in a quantum gas with 3D spin–orbit coupling, *Science* 372(6539), 271 (2021)
18. L. Zeng and J. Zeng, Gap-type dark localized modes in a Bose–Einstein condensate with optical lattices, *Adv. Photonics* 1(04), 046004 (2019)
19. Y. Xu, Y. Zhang, and B. Wu, Bright solitons in spin–orbit-coupled Bose–Einstein condensates, *Phys. Rev. A* 87(1), 013614 (2013)
20. T. F. Xu and C. Zhang, Interference of bright solitons in harmonically trapped pseudo-spin polarization Bose–Einstein condensates, *Chaos Solitons Fractals* 117, 209 (2018)
21. K. Zhou and Z. Zhang, Ground state properties of a two dimensional Fermi superfluid with an anisotropic spin–orbit coupling, *J. Phys. Chem. Solids* 128, 207 (2019)
22. C. Becker, S. Stellmer, P. Soltan-Panahi, S. Dörscher, M. Baumert, E. M. Richter, J. Kronjäger, K. Bongs, and K. Sengstock, Oscillations and interactions of dark and dark–bright solitons in Bose–Einstein condensates, *Nat. Phys.* 4(6), 496 (2008)
23. D. Cao, I. L. Chern, and J. C. Wei, On ground state of spinor Bose–Einstein condensates, *Differential Equations & Applications Nodea.* 18(4), 427 (2011)
24. G. W. Hanson, S. A. Hassani Gangaraj, C. Lee, D. G. Angelakis, and M. Tame, Quantum plasmonic excitation in graphene and loss-insensitive propagation, *Phys. Rev. A* 92(1), 013828 (2015)
25. S. J. Yang, Q. S. Wu, S. N. Zhang, S. Feng, W. Guo, Y. C. Wen, and Y. Yu, Generating ring dark solitons in an evolving Bose–Einstein condensate, *Phys. Rev. A* 76(6), 063606 (2007)
26. D. S. Kharenko, A. E. Bednyakova, E. V. Podivilov, M. P. Fedoruk, and S. A. Babin, Optimization and coherent combining of Raman dissipative solitons in fiber laser, CLEO-Europe, 2015
27. L. X. Wang, C. Q. Dai, L. Wen, T. Liu, H. F. Jiang, H. Saito, S. G. Zhang, and X. F. Zhang, Dynamics of vortices followed by the collapse of ring dark solitons in a two-component Bose–Einstein condensate, *Phys. Rev. A* 97(6), 063607 (2018)
28. M. Kato, X. F. Zhang, and H. Saito, Vortex pairs in a spin–orbit-coupled Bose–Einstein condensate, *Phys. Rev. A* 95(4), 043605 (2017)
29. Y. J. Wang, L. Wen, H. Guo, R. B. Tan, S. G. Zhang, and X. F. Zhang, Spin–orbit-coupled Bose–Einstein condensates in radially periodic potentials, *J. Phys. Soc. Jpn.* 88(2), 024005 (2019)
30. C. F. Liu, Y. M. Yu, S. C. Gou, and W. M. Liu, Vortex chain in anisotropic spin–orbit-coupled spin-1 Bose–Einstein condensates, *Phys. Rev. A* 87(6), 063630 (2013)
31. X. H. Hu, X. F. Zhang, D. Zhao, H. G. Luo, and W. M. Liu, Dynamics and modulation of ring dark solitons in two-dimensional Bose–Einstein condensates with tunable interaction, *Phys. Rev. A* 79(2), 023619 (2009)
32. G. Theocharis, D. J. Frantzeskakis, P. G. Kevrekidis, B. A. Malomed, and Y. S. Kivshar, Ring dark solitons and vortex necklaces in Bose–Einstein condensates, *Phys. Rev. Lett.* 90(12), 120403 (2003)
33. A. L. Fetter, Rotating trapped Bose–Einstein condensates, *Laser Phys.* 18(1), 1 (2008)
34. A. L. Fetter and A. A. Svidzinsky, Vortices in a trapped dilute Bose–Einstein condensate, *J. Phys.: Condens. Matter* 13(12), R135 (2001)
35. V. Pérez-García, M. García-March, and A. Ferrando, Symmetry-assisted vorticity control in Bose–Einstein condensates, *Phys. Rev. A* 75(3), 723 (2012)
36. A. Ferrando, M. Zacarés, M. Á. García-March, J. A. Monsoriu, and P. F. de Córdoba, Vortex transmutation, *Phys. Rev. Lett.* 95(12), 123901 (2005)
37. L. T. Vuong, T. D. Grow, A. Ishaaya, A. L. Gaeta, G. W. 't Hooft, E. R. Eliel, and G. Fibich, Collapse of optical vortices, *Phys. Rev. Lett.* 96(13), 133901 (2006)